# Stability of Buoyant Inverse Diffusion Methane Flames with Confinement Effects

Xuren Zhu, Xi Xia, and Peng Zhang*

Department of Mechanical Engineering

The Hong Kong Polytechnic University, Hung Hom, Hong Kong

## Abstract

Experimental and numerical studies were performed to examine the stability of inverse diffusion flames (IDFs) with the focus on the boundary wall effects. A regime diagram for flame stability was obtained based on the visual characteristics of flames and verified by the simulated flow fields. The boundary wall effects were identified and investigated by simulating the IDFs with different outer burner diameters. It was found that the wall-bounded induced shear flows either reduce the flow instability by vorticity diffusion or enhance it by vorticity convection. Based on the experimental and numerical observations, the mechanism of the boundary wall effects on the stability of buoyant IDFs was explained and further extended to general diffusion flames.

**Keywords:** Inverse diffusion flame; Buoyant flame; Instability; Wall effects; Vortex dynamics.

* Corresponding author. Email address: pengzhang.zhang@polyu.edu.hk (P. Zhang).

# 1. Introduction

Buoyant diffusion flames are common in various industrial combustion devices and accidental fires. Many physical phenomena of fundamental significance are found in buoyancy-driven reactive plumes, for instance vortex transportation and interaction, flow and flame instability, and flow transition to turbulence. Examining the dynamics of buoyant diffusion flames also contributes to applications, such as optimizing combustion efficiency and reducing fire damage. Regardless of the numerous investigations conducted over the past decades [1-10], some processes in buoyant diffusion flames have not been completely understood [11].

Vortex dynamics has been introduced to understand the flow characteristics of buoyant diffusion flames, especially the mechanism of stability. Numerous studies have been done to understand the dynamics of the buoyancy-induced vorticies and the flame/vortex interactions [1, 4, 12-21]. Since the reaction in diffusion flames is dominated by the fuel/oxidizer mixing which is controlled by the transport of vortices, the periodic flickering in buoyant diffusion flames is believed to be closely related to the formation and convection of the large buoyancy-induced toroidal vortices [22-24]. Among others, Jiang and Luo [11, 25] found that the buoyancy-induced large toroidal vortices are responsible for an absolute instability in the downstream of buoyant diffusion flames. In spite of these significant knowledge of flame instability obtained over the past decades, the coupling of chemical heat release, buoyancy, boundary wall effects and other factors in reality urges further understanding of the vortex dynamics mechanisms for different instabilities in buoyant diffusion flames [26].

Inverse diffusion flames (IDFs), which are typically operated in buoyancy-controlled condition due to its relatively small blow-out limit, have been applied as laboratory flames to investigate soot formation especially soot inception for decades [27-30]. Commonly, IDFs burn in a co-flow and

co-annular configuration so that soot forms in the fuel side of the reaction zone, where soot experience inception and surface growth before its agglomeration with other soot particles to form aggregates [27, 30, 31], whereas buoyancy-induced vortices occur in the downstream. These flame features provide an ideal condition for experimental measurements that are designated to model soot formation, especially soot inception and early growth. Due to the special structure of IDFs, such measurements are always performed in the downstream of the flames [27, 31], while flow instability developed in the downstream may cause difficulty to accurate soot sampling. Moreover, IDFs have been recently adopted in synthesizing carbon nanotubes (CNTs) [32, 33], for which an unstable flow may deactivate the catalyst particles by the transportation of polycyclic aromatic hydrocarbons(PAH) or soot to the catalytic substrate, thus impeding the growth or degrading the purity of CNTs [34]. While flow exerts an important influence on soot formation of diffusion flames [29, 35-37], the flow dynamics aspects of IDFs have not been sufficiently studied [38-41].

In a recent work by the authors [42], buoyant methane/air IDFs were investigated to understand the flow dynamics in the near field. It was revealed that for non-reacting flow the interaction between the initial shear flow and buoyancy induces opposite-sign vortices and results in flow instability in the near field, which is similar to that of the von Karman vortex street. A unique characteristic was identified that the near-field instability is most intensified at around unity Richardson number. For reacting flows, the density gradient is reversed by the chemical reaction, hence changing the buoyancy-induced vortex to be of the same sign as that of the initial shear flow. This explains why the near-field instability is suppressed for an IDF. However, it was believed that the initial shear flow would eventually roll up and develop the Kelvin-Helmholtz instability in the downstream, with the assistance of the continuous buoyancy-induced vorticity generation.

The present work is a continuation of our previous work [42], in the sense that it seeks a global perspective of the flame stability of IDFs by answering the question: what occurs to the initial shear flow in the far field? Other than the buoyancy-induced vorticity addition, another major factor to be considered in far field of IDFs is the confinement wall, which is often required to isolate the fuel from the ambient air. The introduction of the confinement gives raise to another problem, namely the effect of the boundary walls on the transportation and interaction of the vortical structures. The wall effects are known to play significant roles in non-buoyant flames [43, 44]. Anderson et al. [45] investigated the interaction between the flame and a constant-temperature wall for non-buoyant diffusion flames. They found that the fuel/oxidizer interface shifted to the cold wall side when the flame stoichiometric mixture fraction was large. Through investigating the interaction of boundary wall with jet flame, Chao and Wu [46] found that the buoyancy-induced vorticity transport, which was affected by the sidewall, plays a major role in shaping the flame structure. They attributed the different flame structures obtained by changing the flame-wall distance to the dissipation effect of the wall on the outer votices. By examining buoyant jet diffusion flames with and without corner wall, Jiang and Luo [47] found that the flame instability is enhanced in the downstream by the deformation and breakdown of the buoyancy-induced large vortical structures owing to vortex interaction with sidewall. To the authors' knowledge, a fundamental and consistent understanding of the wall effect on the stability of buoyant diffusion flames has been lacking, let alone buoyant IDFs.

This study attempts to update the understanding of the wall effects, specifically the associating fundamental vortex dynamics mechanisms, on the stability of an IDF through qualitative experimental observations and then detailed vortex flow analysis based on numerical simulation. Experiment will be first performed to obtain a regime diagram for methane/air IDFs. Then, the comparison between experimental and numerical results will lead to a further investigation of the

flow stability of IDFs in the far field. The role of wall effects in the flame stability will be identified and the detailed mechanism explained by analyzing the evolution and interaction of the vortical structures in the far field. Considering that any flow instability is the result of unsteady behaviors of vortices, which should not be fundamentally different between IDFs and normal diffusion flames (NDFs), the present work would contribute to an improved understanding of the wall effects on the stability of general buoyant diffusion flames.

## 2. Experimental Specifications and Numerical Methodology

As shown in Fig.1, a co-annular burner was designed to generate IDFs. Air flow was injected through the inner tube with a diameter, $d_a$= 0.01 m, while the gaseous fuel (i.e. methane for all cases in the present work) through the outer annular with the diameter of the outer tube, $d_f$= 0.04 m. Thereinafter, non-dimensional distance is applied by using the actual distance divided by the inner tube diameter $d_a$. A quartz glass tube with a length of $l$ = 0.4 m was mounted above the burner base to isolate the ambient air. The air and fuel flows were supplied by pressure vessel and controlled by valves to maintain the inflow conditions at 300K and 101kPa. A Cartesian coordinate system is plotted in Fig. 1 for the convenience of discussion in the following paragraphs. Thermocouple method was used to measure the temperature of the reacting flows to validate the present numerical simulations. As shown in Fig. 1, the thermocouple with a diameter of 5mm and length of 500mm is fixed on a stick holder. The holder is movable in the horizontal direction so that the temperature at varied locations on the burner axis can be measured. For more detailed information of the air and fuel supply systems, experimental set-ups and the flame image capture system, the interested readers are referred to a recent work by the authors [42].

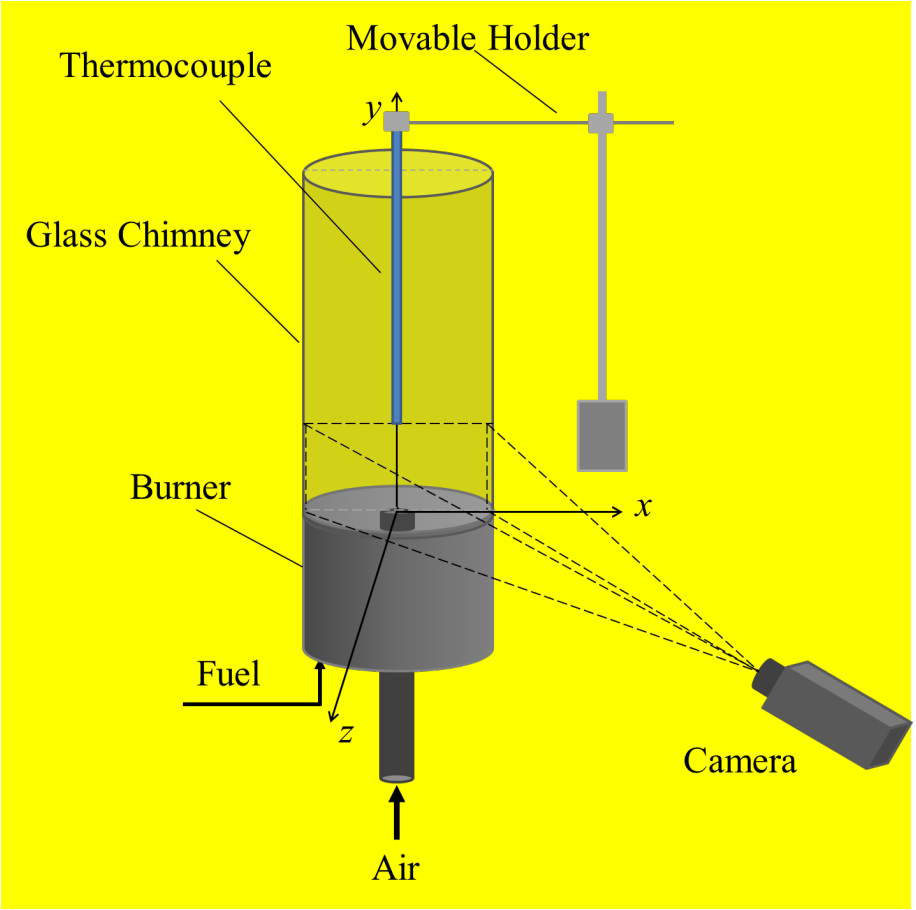


Figure 1: Experimental specifications.

Large eddy simulation (LES) was also conducted to investigate the IDF flow through the open source code, OpenFOAM [48]. The unsteady Navier-Stokes equations were solved by Pressure and momentum correctors combined with the Pressure Implicit with the Splitting of Operators (PISO) method [49]. The spatial and unsteady terms were discretized by second order schemes [50, 51]. Second order central difference linear interpolation was applied for mass flux calculation. The time step was limited by Courant-Friedrichs-Lewy (CFL) number with the value of 0.4 for non-reacting cases and 0.3 for reacting cases to reduce the simulation oscillation. The well documented one-equation eddy viscosity model was applied to treat the filtered sub-grid term [52-54] The computational mesh of the burner for a representative case is shown in Fig. 2. The number of total grid nodes is 0.6 million with local refinement in the vicinities of the fuel-air interfaces as well

as the solid wall and the grid size varies in the range of $0.01d_a$ – $0.12d_a$. The infinitely fast and irreversible chemical reaction schemes were coupled with the flow solver to calculate the flow and temperature field. More detailed numerical methodology is provided in Ref. [42].

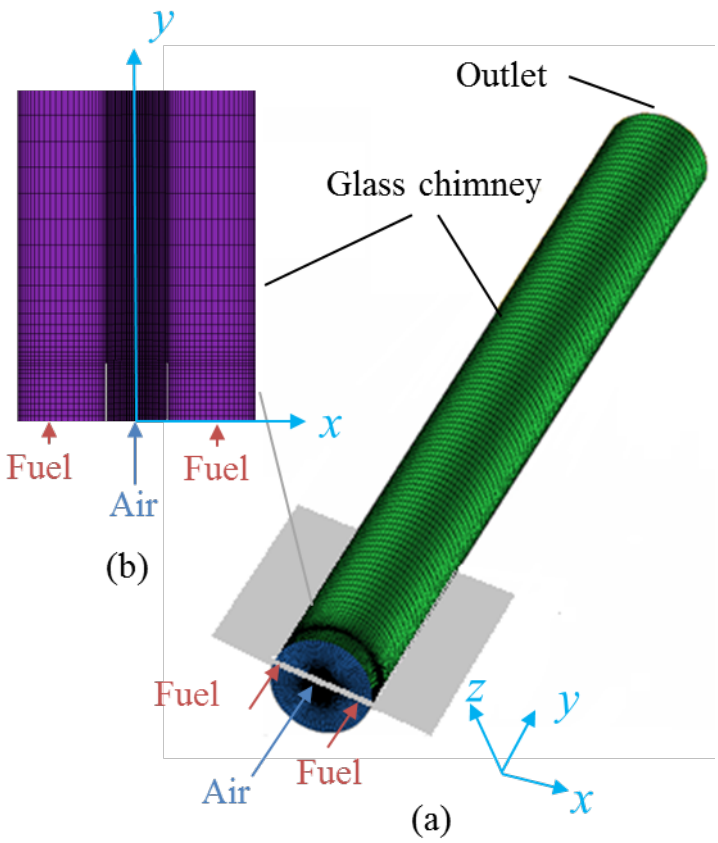


Figure 2: (a) 3-D computational mesh and (b) magnified view of the mesh near the air inlet.

The boundary conditions are shown in Table 1 for the numerical simulation. Uniformed velocity profiles were used for the inflow conditions of air and fuel flow. To determine the temperature boundary condition on the side wall, the temperature at different vertical locations of the glass tube was measured experimentally. As the standard deviation is only about 37K, the averaged value of 450K was used in the present simulation for simplicity.

Table 1: Boundary conditions for the benchmark reacting IDF case

| | Velocity (m/s) | Pressure (Pa) | Temperature (K) | Components (-) |
|---|---|---|---|---|
| Air inlet | Fixed value/Uniform | Zero Gradient | 300 | 100% air |
| Fuel inlet | Fixed value/Uniform | Zero Gradient | 300 | 100% Methane |
| Outlet | Zero Gradient | 101325 | Zero Gradient | Zero Gradient |
| Glass chimney | 0 | Zero Gradient | 450 | Zero Gradient |

## 3. Validation of Simulation for Reacting IDFs

In the present work, the burner has a fixed configuration, with an outer-to-inner diameter ratio $k = d_f/d_a = 4$. Thus, the controlling parameters are the flow rates of the injecting air and fuel, which result in two non-dimensional flow parameters, namely the air flow Reynolds number, $Re_a$, and the fuel flow Reynolds number, $Re_f$, and an overall fuel/air ratio, $\Phi$, as a non-dimensional measure of the relative abundance of fuel compared with air:

$$Re_a = \frac{\rho_a v_a d_a}{\mu_a},\ Re_f = \frac{\rho_f v_f d_a}{\mu_f},\ \text{and}\ \Phi = 2(Q_f/Q_a), \quad (1)$$

where $\rho$, $v$, and $\mu$ are the density, velocity, and dynamic viscosity, respectively. $Q$ is the molar flow rate. The subscript $a$ and $f$ represent the properties of the air and fuel flows, respectively. In the present study, the defined Reynolds number is about 100-500, the corresponding Kolmogorov micro scale $l_o = lRe^{-3/4}$ is about 0.004m, and the mesh size $\Delta \leq 0.12d_a = 0.0012m$, which is actually fine enough to perform LES.

Comprehensive validation including grid independence study has been performed in Ref. [42]; here, we provide additional validation for the reacting IDFs. Since for diffusion flames which are controlled by fuel/oxidizer mixing, flame height represents one of the most important flame characteristics [55], the current work used the experimentally measured flame height to validate the

simulation results. According to Mikofski et al. [30], the edge of the blue flame approximates the reaction zone of methane/air IDFs, which is characterized by a local temperature peak. The flame height in the experiments is obtained by measuring the distance from the blue flame tip to the center of the burner exit, whereas the numerical flame height is determined as the distance between the location of maximum temperature on the axis and the center of burner exit. As shown in Fig. 3 (a), the blue flame outlines of the experimental images show qualitative agreement with the peak temperature contours of the simulation results, demonstrating a general good performance of our simulation in capturing the flame characteristics. Here, $\tilde{T} = \frac{T}{T_0} = \frac{T}{300K}$ is the non-dimensional temperature. The validity of our simulation can be further justified by Fig.3 (b), which compares the flame height $H$ between experiment and simulation.

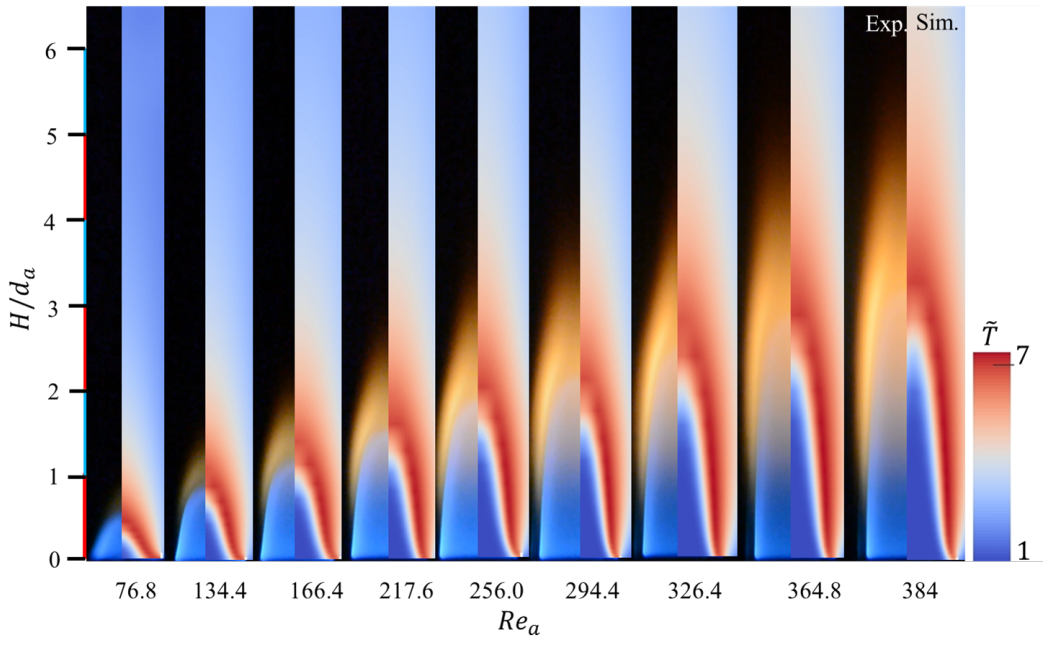


(a)

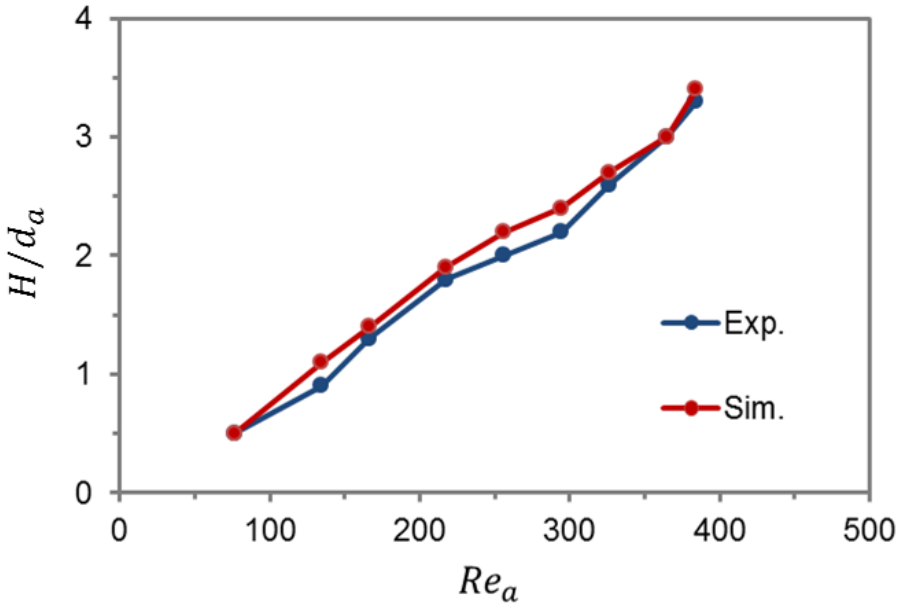


(b)

Figure 3: (a) comparison between experimental flame images and simulated temperature contour, and (b) comparison of averaged flame height for IDFs with $Re_f = 34.8$ and various $Re_a$. Exp. for experiment and Sim. for simulation.

For a quantitative validation, the comparison of temperature variation along the burner axis between measured and numerical results in a representative IDF is shown in Fig. 5. Since the intrusive thermocouple method may distort the small IDF, probing locations are set in the downstream of the flame. The temperature results have been corrected by the radiation heat loss of the thermocouple[56, 57]. Considering that soot deposition and other factors may inevitably affect the measurement[56, 58], experimental uncertainties are estimated and indicated in the figure. Fig. 4 shows a good agreement indicating that the high fidelity numerical simulation has been achieved.

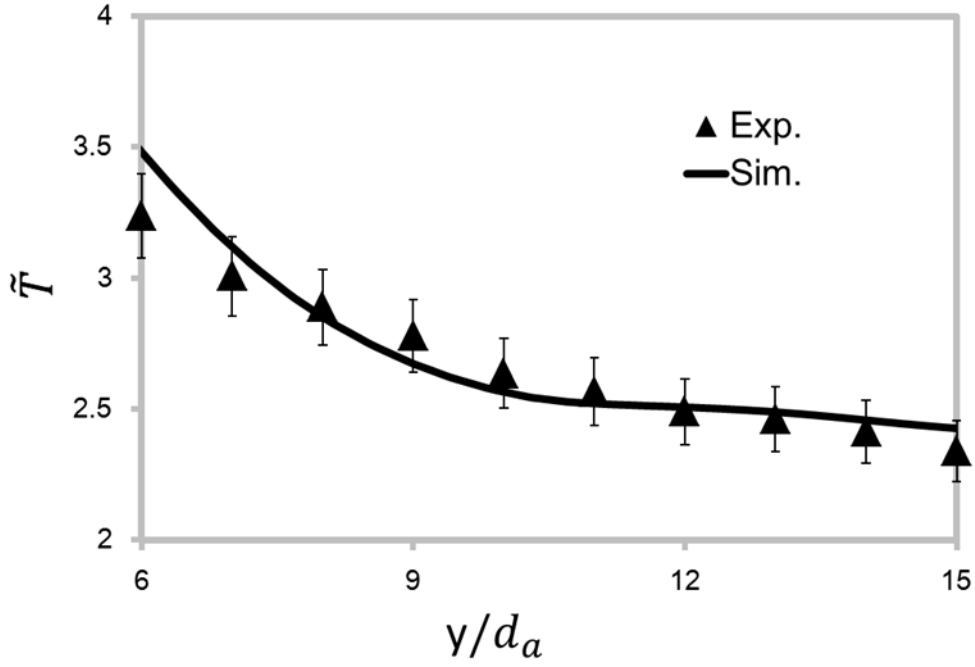


Figure 4 Comparison of the temperature variation along the burner axis for the case with $Re_a = 294.4$ and $Re_f = 34.8$. Exp. and Sim. are for measured and numerical results respectively. $\tilde{T}$ is the non-dimensional temperature, $y/d_a$ is the non-dimensional axial location.

## 4. Stability Regime Diagram of Methane IDFs

By following the work by Wu and Essenhigh [41], we first report the experimental stability regimes of IDFs in Fig. 5. It is noted that the flames in the regime diagram were classified based on their visual appearances, thereby Fig. 5 only provides general description on the qualitative characteristics of methane IDFs to bring up the later discussion on the flame dynamics of IDFs in the far field. The boundary lines separating the different regimes were obtained by fine tuning the fuel or air flow rates based on a coarser sampling mesh, the representative data points of which are shown in Fig. 5. The boundary differentiating the main stability regimes is plotted by the red line, above which

IDFs are stable and below are unstable. Five different regimes of IDFs were identified based on their visual appearance, as are summarized below.

(1) *Regime I*: Stable; blue flame at the bottom and faint yellow cap right above the blue region; increasing $Re_f$ causes no notable change in flame appearance.

(2) *Regime II*: Unstable; flame has a slight swaying and flicking; blue flame with a faint yellow cap, similar to Regime I.

(3) *Regime III*: Stable; brighter and more extended yellow flame region than Regime I; flame height increases with $Re_a$ in a roughly linear pattern; increasing $Re_f$ slightly decreases flame height and causes no significant change in flame appearance.

(4) *Regime IV*: Unstable; notable flame swaying and flickering identified; the swaying amplitude of the visual flame increases with increasing $Re_a$ or decreasing $Re_f$.

(5) *Regime V*: Unstable; dim blue flame without yellow flame; notable swaying and flickering of the blue flame identified; with sufficiently large $Re_a$, over-ventilated flame occurs.

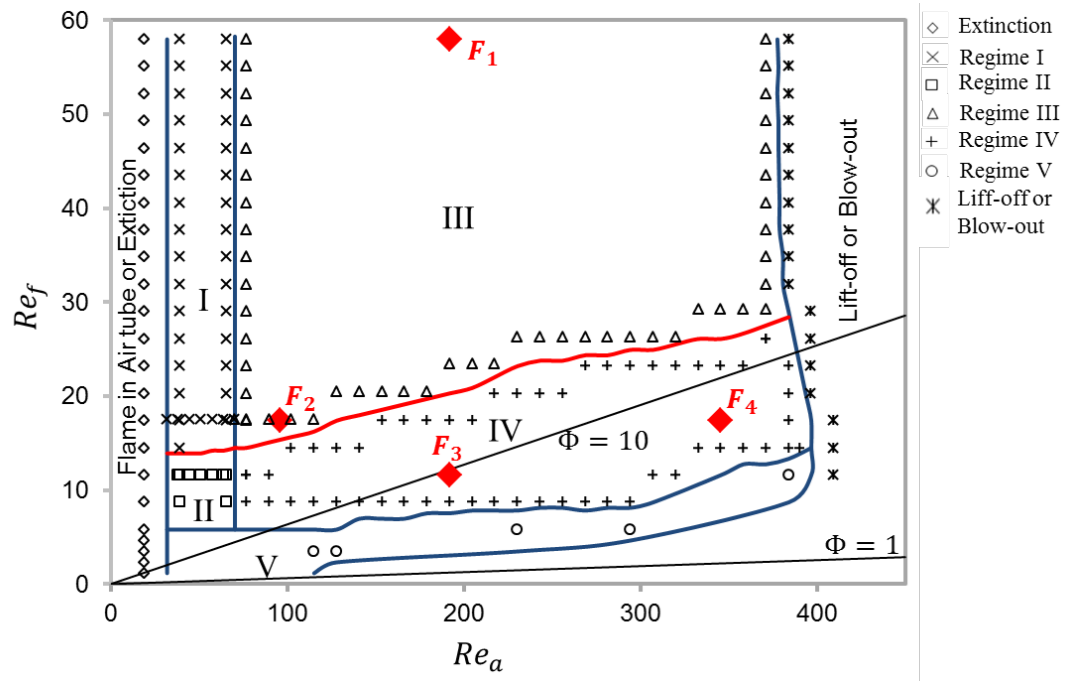


Figure 5: IDF regime diagram for the burner with $k = 4$. The red line is the boundary between stable and unstable IDFs, and $\Phi$ is the overall fuel/air ratio.

It is noted that Fig. 5 generally agrees well the regime diagram provided by Wu and Essenhigh [41]. The main difference between the two regime diagrams is the different flame characteristics at low $Re_f$, where the flame is sensitive to slight variation of fuel or air inflow. Regardless of the slight difference, the most representative stable (III) and unstable (IV) regimes are captured in both regime diagrams. Fig. 5 shows that the IDFs tend to become more stable with decreasing $Re_a$ or increasing $Re_f$. Furthermore, $Re_a$ shows a predominant effect on the flame height, the size of yellow flame, and the radiation intensity, which are less sensitive to $Re_f$. This is because with the present burner geometry and dimensions (especially the diameter ratio $k = 4$), flames of most regimes are globally "fuel rich" according to the iso-lines of $\Phi$ in Fig. 5, meaning that fuel is sufficient in regimes above the $\Phi = 1$ line while air is consumed completely. Thus, further increasing the fuel flow rate (or $Re_f$) would not significantly affect the flame properties that are dictated by the chemical reaction.

As shown in Fig. 1, the present experiment is unable to resolve the entire flow field simultaneously. As a remedy, we adopt validated numerical simulation to provide the instantaneous flow field globally. Fig. 6 presents the comparisons between instantaneous experimental flame images and simulated temperature fields for four representative cases. As shown in Fig. 6, the four benchmark cases belong to Regime III and Regime IV, which are the most representative stable and unstable IDF regimes, respectively. The inlet conditions for the four IDFs are:$F_1$ $(Re_a = 192, Re_f = 58)$ ; $F_2$ $(Re_a = 96, Re_f = 17.4)$ ; $F_3$ $(Re_a = 192, Re_f = 11.6)$ ; $F_4$ $(Re_a = 345.6, Re_f = 17.6)$ . Hereinafter, the IDF has the same $Re_a$ and $Re_f$ with $F_1$ will be marked as $F_1$, and so forth.

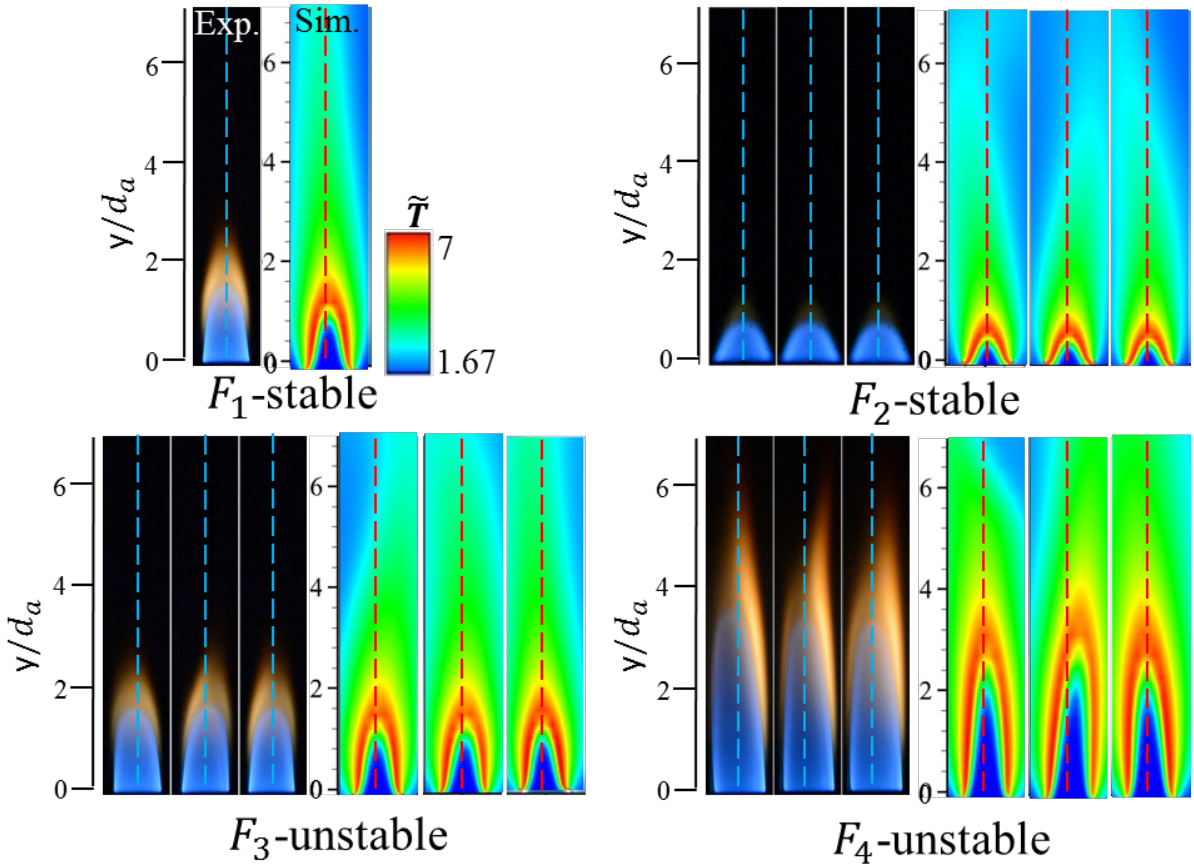


Figure 6: Instantaneous experimental and numerical flame images for the four IDFs ($F_1 - F_4$) highlighted in Fig. 5. Exp. for experiment and Sim. for simulation.

Although the stability of IDFs is described based on the visual flames, we need to consider the entire flow field to understand the fundamental mechanism. This is because, as the flow moves downstream of the flame, the transition to an unstable flow is often inevitable, even for the case with a stable visual flame, e.g., the unstable flow structure downstream of the flame evident from the simulated temperature field of $F_2$. Since the development of instability often originates from the far field and then gradually propagates to the near field, we deem the flow instability occurring downstream to be of essential importance. The flow field of the four IDFs is further investigated in a global sense in Fig. 7, which plots the contours of the $z$-direction vorticity ($\Omega_z$) and the temperature in a three-dimensional view. The z-direction vorticity is defined as $\boldsymbol{\Omega}_z = \left(\frac{\partial U_y}{\partial x} - \frac{\partial U_x}{\partial y}\right)\vec{k}$, where $U_y$ and $U_x$ are the velocity components in the $y$ and $x$ direction respectively, and $\vec{k}$ is the unit vector in the $z$ direction. In the vorticity contours, two shear flows of opposite-sign vorticity are generated due to the velocity difference between the inner and outer flow at the burner inlet. By examining the shear flow structure, It is observed that the two shear flows remain relatively stable in the near field, the detailed mechanism for which has been explained in our previous work [42]. However, as the two shear flows evolve downstream, they eventually turn to unstable modes for all cases except $F_1$. This indicates that an IDF with higher fuel inlet velocity for given air inlet velocity case or smaller velocity difference (e.g. $F_1$) tends to become more stable in the far field. The above numerical finding also agrees well with our experimental observations from the flame regime diagram in Fig. 5, confirming that the flow field downstream plays a significant role in the stability of buoyant IDFs. Thus, to obtain a comprehensive understanding of the wall effects on flow stability and the associated mechanisms, a vortex-dynamics investigation focusing on the far field of IDFs will be presented in the next section.

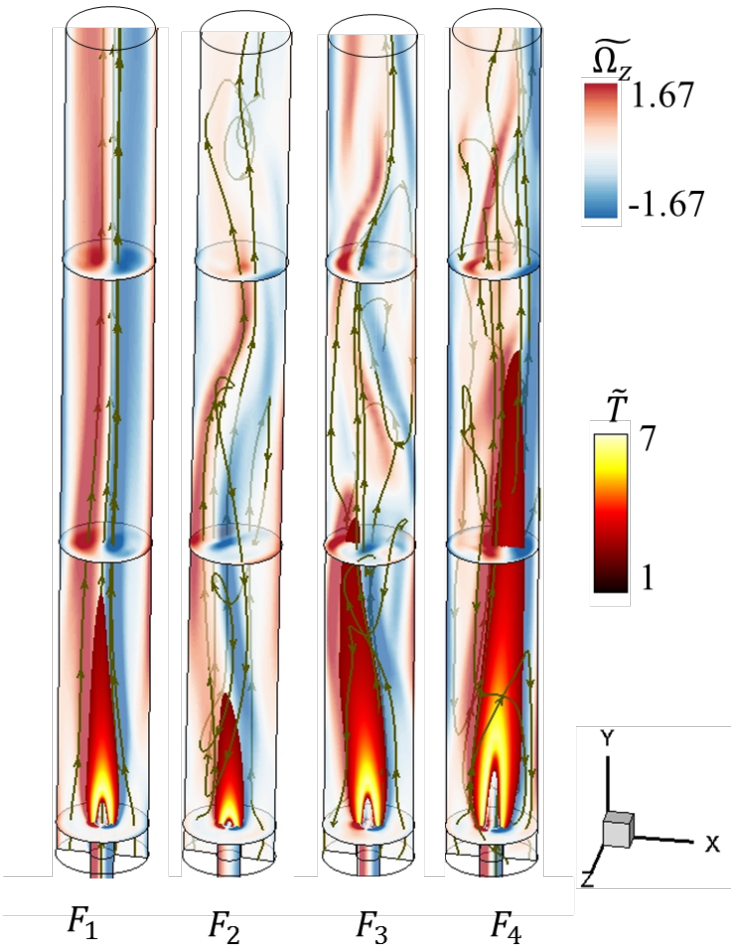


Figure 7: Instantaneous flow field (denoted by the contour of $z$-direction vorticity) and flame structure (denoted by the temperature contour) for the four IDFs ($F_1 - F_4$) highlighted in Fig. 5.

$$\widetilde{\Omega_z} = \frac{\Omega_z}{60(1/s)} \text{ and } \tilde{T} = \frac{T}{300K}.$$

## 5. Boundary Wall Effects on the Stability of IDFs

### 5.1. Wall Effects of an IDF from Vortex Dynamics Perspective

In general, a diffusion flame sheet corresponds to a thin layer where fuel and oxidizer encounter and react with each other. As the reactants are transported to the flame sheet through convection and diffusion, any dynamic behavior of the luminous flame reflects the unsteadiness of its associating flow field, which usually involves vortices. For buoyancy-driven diffusion flames, the flame oscillation has been attributed to the formation and convection of the large vortical structures [1, 59],

where the vorticity is generated by a combined effect of gravity and density gradient [11, 16, 24]. The same buoyancy-induced mechanism should also account for the vorticity generation of the current IDFs. One major difference, however, originates from the addition of the solid-wall confinement, which is practically necessary to isolate the fuel flow of an IDF from its ambient air environment. To this end, the current work seeks to understand the effect of the confinement wall from the vortex dynamics perspective.

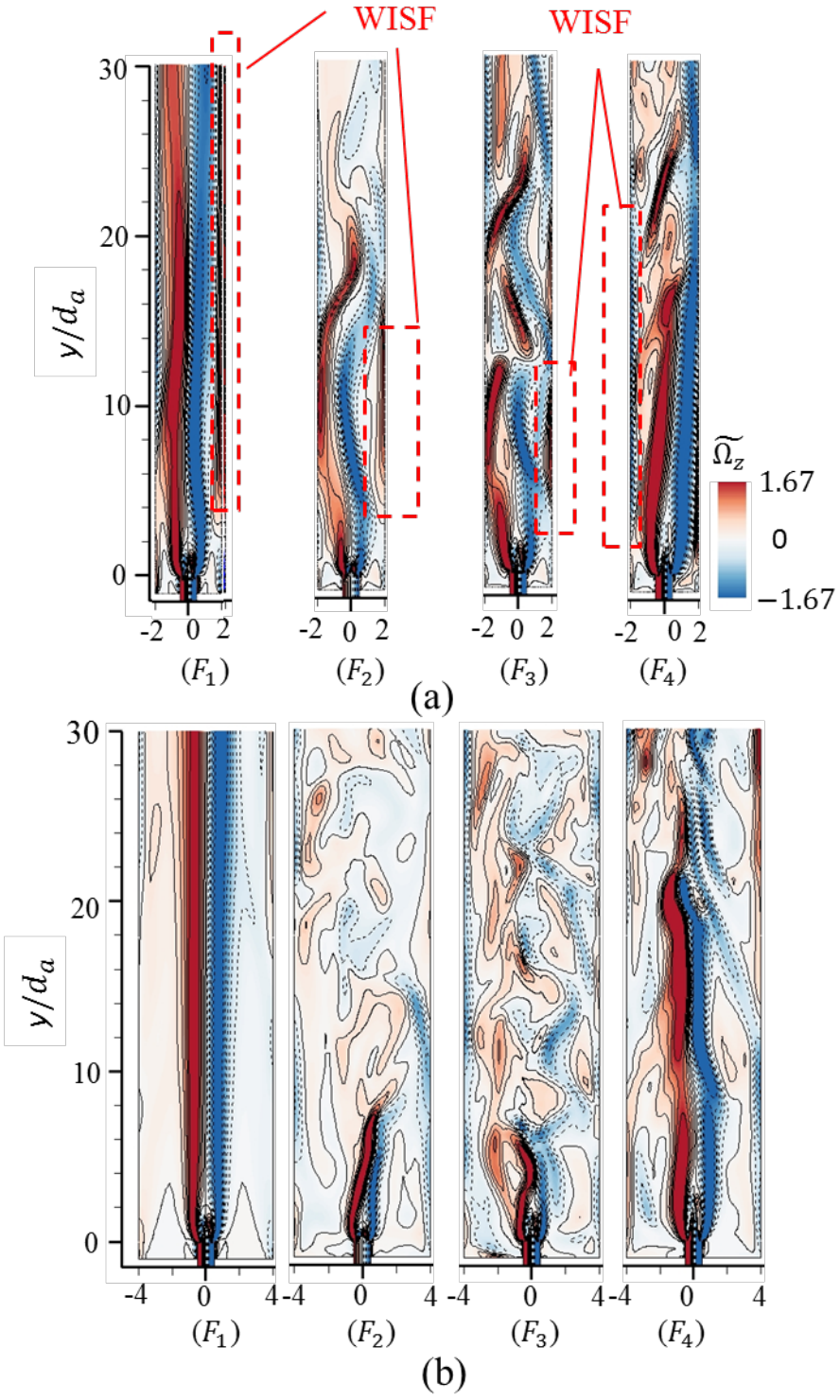


Figure 8: Instantaneous $z$-direction vorticity $\Omega_z$ contours for $F_1$-$F_4$ (a): $k = 4$; (b): $k = 8$ ($k = d_f/d_a$ is the outer-to-inner diameter ratio). The WISFs are marked by the dashed boxes.

We start by analyzing the flow stability of the IDFs in Fig. 8. The contours of the $z$-direction vorticity, $\Omega_z$, in the $xy$ plane are plotted for cases $F_1$-$F_4$ in Fig. 8 (a). In each case, two initial shear flows with opposite-direction vorticity grow along the flame as they convect downstream, thanks to the buoyancy-induced vorticity generation. It can be observed that, in all cases, the region of stable luminous flame of Fig. 5 approximately matches with the region of symmetric shear layers of Fig. 8(a), verifying the relevance between vortices and flame stability. However, the center shear flows seem to become unstable in the further downstream, even for case $F_1$ that has an apparent stable luminous flame. Judging from the downstream shear flows, which are in close contact with the side walls, we hypothesize that this flow instability is caused by the wall effects. A direct evidence is the emergence of a wall-bounded induce shear flows (WISF), as illustrated in Fig. 8(a), that is generated due to the induced effect of an existing vortex or shear flow approaching the wall. The mechanism generating the WISF has been well understood by previous studies of vortex-wall interactions [60-62]. Basically, a primary shear flow would always induce a crossflow along its adjacent solid boundary in the inviscid sense. Due to the non-slip boundary condition, the inviscid crossflow of the primary shear flow has to be decelerated at the wall, thus resulting in the formation of a boundary layer on the wall surface, which is the WISF. It is interesting to note that the vorticity inside the WISF is intrinsically opposite to the primary shear flow. Next, we shall discuss the detailed interactions between the WISFs and the primary shear flows to understand the subsequent effects on the stability of IDFs.

### 5.2. Wall Effects on Flow Stability of IDFs

From vortex dynamics perspective, the effect of a vortical structure on its ambient flow is generally two folds, namely convective and diffusive. The convective effect can be thought as a

superimposed velocity field on the original flow without the vortex; whereas the diffusive effect can be considered as an added source or sink of vorticity. Thus, the convective effective is likely to cause the disturbance on vorticity transport while the diffusive effect causes vorticity addition or annihilation. For the WISF considered in the current study, its fundamental principle should not be different from that of a general vortical structure.

In order to examine in detail the convective and diffusive effects of the WISF, we need to compare the current IDFs to reference cases that have no wall effects or at least reduced wall effects. For this purpose, four additional cases were simulated for an enlarged burner with $k$ = 8 as shown in Fig. 8 (b), while their other conditions being identical to cases $F_1$-$F_4$, respectively. It is noted that the enlarged burner corresponds to an increased effective Φ, which however generates no obvious influence on the chemical properties of the IDFs since they are already "fuel rich" according to Section 4. The results of vorticity contours for the $k$ = 8 cases are presented Fig. 8(b). To provide a quantitative judgement of the stability for the IDFs in Fig. 8, the variations of turbulence intensity along the center line are plotted in Fig. 9. Here, the turbulence intensity is defined as $I = \frac{u'}{U}$, where $u'$ is the root mean square of the turbulent velocity fluctuations and $U$ is the Reynolds averaged mean velocity.

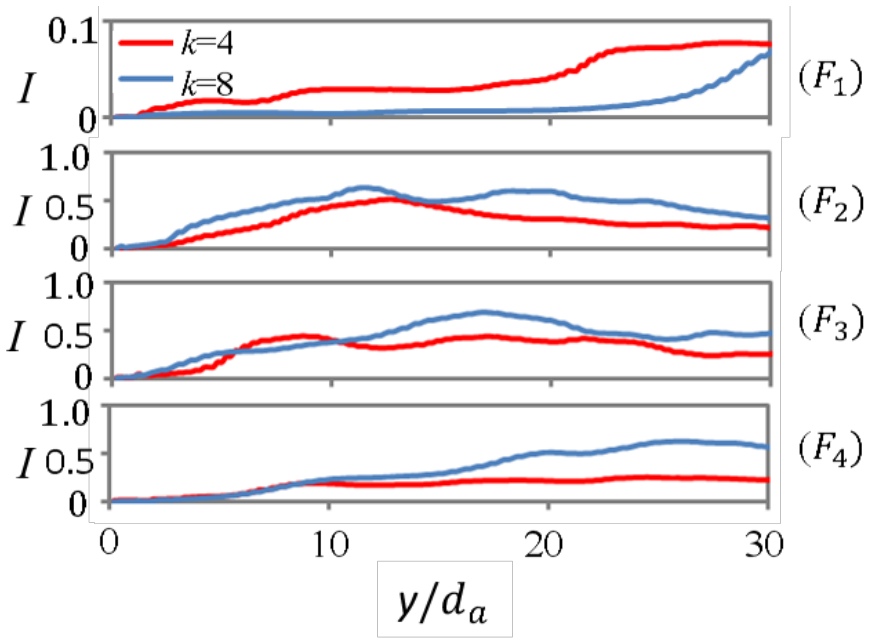


Figure 9: Comparison of turbulence intensity variation along the center line for $F_1$-$F_4$ with red line: $k$=4; dashed blue line: $k$=8.

We first compare the two cases, $k = 4$ and $k = 8$, of $F_1$. It is observed that the flow corresponding to $k = 8$ is rather stable throughout the entire flow field and no notable structure can be identified near the wall. The $k = 4$ case, on the other hand, has slightly sinuous center shear flows, displaying a less stable flow compared with the $k = 8$ case. This observation is also supported by the turbulent intensity calculations of $F_1$ in Fig. 9. Since the apparent difference between the two vorticity contours is the asymmetric WISFs generated near the side wall of the smaller burner, the effect of the WISF in this case should be understood as convective, which cause small disturbances to the main shear flows.

For the cases corresponding to $F_2$-$F_4$ in Fig. 8(b), the flow become much more unstable than $F_1$ because of either an enhanced initial shear flow ($F_2, F_3$) or an increased buoyancy-induced vorticity generation due to elongated flame ($F_4$). By comparing Fig. 8(a) and Fig. 8(b), the stronger WISFs of cases $F_2$-$F_4$ in Fig. 8(a), induced by main shear flows that are closer to the walls, seem to

cause a less intense breakdown of vortices or a weaker turbulence as indicated from Fig. 9. This suggests that stronger WISFs tend to stabilize the main shear flows for cases $F_2$-$F_4$, which could be explained by the diffusive effect of the WISFs as follows. Recall that a WISF and its associating main shear flow have opposite-sign vorticities, according to the vorticity diffusion term, $\nu\nabla^2\omega$, in the vorticity transport equation [47], the vorticity diffusion serve as vorticity sink to deplete vorticity in both shear flows, and the effect intensifies as the shear flows become closer to each other. In the cases of the larger burner where the main shear flows are initially farther away from the boundary wall, the wall effects are relatively weak so the main shear flows are able to grow and roll up into large vortices, which then detaches from the main shear flows and interacts with the wall to create a highly unstable downstream flow; this is evident from the segmental vortical structures in Fig. 8(b). However, in the cases of the smaller burner, the closer distance between the main shear flows and the wall causes strong WISFs, the diffusion effect of which prevents the growth and roll-up of the main shear flows during the early-stage development. As a result, the main shear flows of $F_2$-$F_4$ in Fig. 8(a) remain rather intact or at least less disturbed compared with those in Fig. 8(b).

The above findings can be interpreted below. For an initially stable IDF, the introduction of side wall would cause WISFs that affect the main flow through convection and impair the established flow stability. For an initially unstable IDF, stronger WISFs would help restrain the continuous growth of the main shear flow and suppress vortex roll-up and detachment, which eventually contributes to a more stable downstream flow. This understanding can be further illustrated by the schematic shown in Fig. 10, where each circle with arrow represents a vortex. The red and blue colors denote the positive and negative signs of the z-direction vorticity, respectively. Fig. 10 (a) illustrates the generation mechanism of main shear flows (MSFs), which is caused by the velocity difference between the inner and outer flows at the burner inlet, regardless of whether boundary wall

presents. Under the gravitational effect, the strengths of the two MSFs would keep growing as they convect downstream. In the presence of the boundary wall as shown in Fig. 10 (b), the enhanced MSFs would induce the generation of the WISFs in the vicinity of the wall. As discussed previously, the interaction between the WISFs and the MSFs by vorticity convection or diffusion either destabilizes or stabilizes the flow field, depending on the original stability of the unbounded flame. It should be emphasized that since the generated WISFs have opposite direction to their corresponding MSFs and an unbounded IDF flow is usually unstable, vorticity diffusion from WISFs to MSFs is the main mechanism for the stabilization of most IDFs in the present study (e.g. $F_2 - F_4$ in Fig. 8).

Last, the mechanism depicted in Fig. 10 also provides a compelling explanation for the flame/wall interaction of jet flames studied by Chao and Wu [46]. Their work showed that the flame length increases as the gap between the sidewall and the flame closes down. This phenomenon can be understood by the present mechanism that, as the flame and the wall approach each other, the vorticity diffusion from the flame-bounded shear flow to the wall-bounded shear layer is enhanced, thus restraining the growth and evolution of the flame-bounded shear flow. As a result, the roll-up of the shear flow into large vortices is postponed so that the shear flow maintains relatively stable and sustains a longer flame. The above analysis suggests that the understanding of the wall effects on flame stability gained from IDFs can be extended to general diffusion flames.

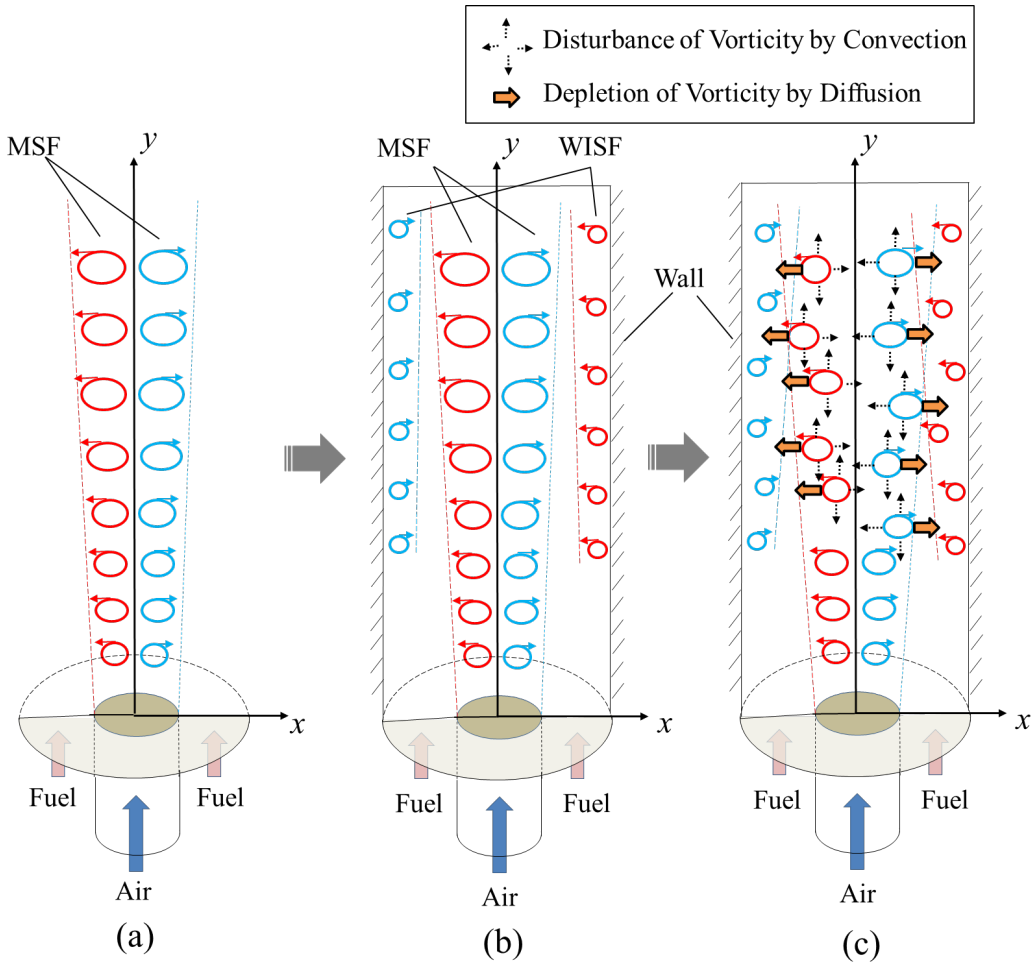


Figure 10: Schematic of the wall effects on the stability of buoyant IDFs: (a) generation of MSF; (b) WISF induced by MSF, (c) The effect of vorticity diffusion and convection on MSF caused by WISF. MSF: main shear flow; WISF: wall induced shear flow. Red circles with arrow denote positive $z$-direction vorticity ($\Omega_z > 0$) and blue for negative $z$-direction vorticity ($\Omega_z < 0$).

## 6. Concluding Remarks

In the present work, methane inverse diffusion flames (IDFs) were investigated to understand the wall effects on the stability of the flame and flow. The visual flame characteristics of the IDFs were studied experimentally and summarized in a regime diagram. The representative stable and unstable modes identified from the regime diagram were also confirmed by numerical simulation. Through physically delineating the simulated flow field of IDFs, a wall-bounded induced shear flow

(WISF) was identified to account for the main wall effects. The IDFs generated from an enlarged burner were numerically found to have minor wall effects. By analyzing the vorticity transportation, we found that the WISFs of the small-burner IDFs may cause either vorticity convection or vorticity diffusion. Specifically, if the original minor-wall-effect IDF is stable then the WISFs would destabilize the flow because of the disturbances introduced by vorticity convection. However, for originally unstable minor-wall-effect IDFs, the vorticity diffusion from the WISFs would stabilize the flow by restraining the development of the main shear flows, and consequently suppressing the roll-up and detachment of individual vortices. This contributes to a fundamental understanding of the wall effects on the stability of IDFs, which can be extended to explain the more general flame/wall interaction in a diffusion flame.

**Acknowledgement**

This work was supported partly by National Natural Science Foundation of China (Grant No. 91641105) and partly by the Hong Kong Polytechnic University (G-UA2M, G-YBGA, and G-YBXN).

**References**

[1] L.D. Chen, J.P. Seaba, W.M. Roquemore, L.P. Goss, Buoyant diffusion flames, Proc. Combust. Inst. 22 (1989) 677-684.

[2] D. Durox, T. Yuan, E. Villermaux, The effect of buoyancy on flickering in diffusion flames, Combust. Sci. Technol. 124 (1997) 277-294.

[3] B.M. Cetegen, Y. Dong, Experiments on the instability modes of buoyant diffusion flames and effects of ambient atmosphere on the instabilities, Exper. Fluids 28 (2000) 546-558.

[4] A. Liñán, M. Vera, A.L. Sánchez, Ignition, liftoff, and extinction of gaseous diffusion flames,

Annu. Rev. Fluid Mech. 47 (2015) 293-314.

[5] S.R. Tieszen, V.F. Nicolette, L.A. Gritzo, J.L. Moya, J.K. Holen, D. Murray, Vortical structures in pool fires: Observation, speculation, and simulation, Sandia National Labs., Albuquerque, NM (United States), 1996.

[6] S.R. Tieszen, On the fluid mechanics of fires, Annu. Rev. Fluid Mech. 33 (2001) 67-92.

[7] H. Gotoda, Y. Asano, K.H. Chuah, G. Kushida, Nonlinear analysis on dynamic behavior of buoyancy-induced flame oscillation under swirling flow, Int. J. Heat Mass Tran. 52 (2009) 5423-5432.

[8] A.Y. Snegirev, J. Marsden, J. Francis, G. Makhviladze, Numerical studies and experimental observations of whirling flames, Int. J. Heat Mass Tran. 47 (2004) 2523-2539.

[9] F. Tang, L. Hu, Q. Wang, Z. Ding, Flame pulsation frequency of conduction-controlled rectangular hydrocarbon pool fires of different aspect ratios in a sub-atmospheric pressure, Int. J. Heat Mass Tran. 76 (2014) 447-451.

[10] Z. Yan, G. Holmstedt, A two-equation turbulence model and its application to a buoyant diffusion flame, Int. J. Heat Mass Tran. 42 (1999) 1305-1315.

[11] X. Jiang, K.H. Luo, Combustion-induced buoyancy effects of an axisymmetric reactive plume, Proc. Combust. Inst. 28 (2000) 1989-1995.

[12] R.W. Davis, E.F. Moore, R.J. Santoro, J.R. Ness, Isolation of buoyancy effects in jet diffusion flame experiments, Combust. Sci. Technol. 73 (1990) 625-635.

[13] J. Carpio, M. Sánchez-Sanz, E. Fernández-Tarrazo, Pinch-off in forced and non-forced, buoyant laminar jet diffusion flames, Combust. Flame 159 (2012) 161-169.

[14] V.R. Katta, W.M. Roquemore, Role of inner and outer structures in transitional jet diffusion flame, Combust. Flame 92 (1993) 274-282.

[15] V.R. Katta, L.P. Goss, W.M. Roquemore, Numerical investigations of transitional H2/N2 jet diffusion flames, AIAA journal 32 (1994) 84-94.

[16] A.F. Ghoniem, I. Lakkis, M. Soteriou, Numerical simulation of the dynamics of large fire plumes and the phenomenon of puffing, Proc. Combust. Inst. 26 (1996) 1531-1539.

[17] J. Jiin-Yuh, C. Wen-Jeng, Vortex instability of buoyancy-induced inclined boundary layer flow in a saturated porous medium, Int. J. Heat Mass Tran. 31 (1988) 759-767.

[18] C.C. Huang, T.F. Lin, Buoyancy induced flow transition in mixed convective flow of air through a bottom heated horizontal rectangular duct, Int. J. Heat Mass Tran. 37 (1994) 1235-1255.

[19] G. Biswas, S. Sarkar, Effect of thermal buoyancy on vortex shedding past a circular cylinder in cross-flow at low Reynolds numbers, Int. J. Heat Mass Tran. 52 (2009) 1897-1912.

[20] D. Chatterjee, B. Mondal, Effect of thermal buoyancy on vortex shedding behind a square cylinder in cross flow at low Reynolds numbers, Int. J. Heat Mass Tran. 54 (2011) 5262-5274.

[21] M.C. Smith, D.A. Haines, W.A. Main, Growth of buoyancy-induced longitudinal vortex pairs in a laminar flow, Int. J. Heat Mass Tran. 32 (1989) 1879-1885.

[22] L.D. Chen, W.M. Roquemore, Visualization of jet flames, Combust. Flame 66 (1986) 81-86.

[23] J.L. Ellzey, E.S. Oran, Effects of heat release and gravity on an unsteady diffusion flame, Proc. Combust. Inst. 23 (1991) 1635-1640.

[24] Z. Shu, S.K. Aggarwal, V.R. Katta, I.K. Puri, Flame-vortex dynamics in an inverse partially premixed combustor: The Froude number effects, Combust. Flame 111 (1997) 276-295.

[25] X. Jiang, K. Luo, Spatial direct numerical simulation of the large vortical structures in forced plumes, Flow Turbulence Combust. 64 (2000) 43-69.

[26] C.M. Coats, Coherent structures in combustion, Prog. Energy Combust. Sci. 22 (1996) 427-509.

[27] G.W. Sidebotham, I. Glassman, Flame temperature, fuel structure, and fuel concentration effects on soot formation in inverse diffusion flames, Combust. Flame 90 (1992) 269-283.

[28] A. Sobiesiak, J.C. Wenzell, Characteristics and structure of inverse flames of natural gas, Proc. Combust. Inst. 30 (2005) 743-749.

[29] C.R. Kaplan, K. Kailasanath, Flow-field effects on soot formation in normal and inverse methane–air diffusion flames, Combust. Flame 124 (2001) 275-294.

[30] M.A. Mikofski, T.C. Williams, C.R. Shaddix, L.G. Blevins, Flame height measurement of

laminar inverse diffusion flames, Combust. Flame 146 (2006) 63-72.

[31] G.W. Sidebotham, I. Glassman, Effect of oxygen addition to a near-sooting ethene inverse diffusion flame, Combust. Sci. Technol. 81 (1992) 207-219.

[32] F. Xu, X. Liu, D.T. Stephen, Synthesis of carbon nanotubes on metal alloy substrates with voltage bias in methane inverse diffusion flames, Carbon 44 (2006) 570-577.

[33] G.W. Lee, J. Jurng, J. Hwang, Formation of Ni-catalyzed multiwalled carbon nanotubes and nanofibers on a substrate using an ethylene inverse diffusion flame, Combust. Flame 139 (2004) 167-175.

[34] C.J. Unrau, R.L. Axelbaum, P. Biswas, P. Fraundorf, Synthesis of single-walled carbon nanotubes in oxy-fuel inverse diffusion flames with online diagnostics, Proc. Combust. Inst. 31 (2007) 1865-1872.

[35] C.R. Shaddix, T.C. Williams, Measurements of the velocity field in laminar ethylene inverse jet diffusion flames, Combust. Flame 156 (2009) 942-945.

[36] C.B. Saji, C. Balaji, T. Sundararajan, Investigation of soot transport and radiative heat transfer in an ethylene jet diffusion flame, Int. J. Heat Mass Tran. 51 (2008) 4287-4299.

[37] C.R. Shaddix, Á.B. Palotás, C.M. Megaridis, M.Y. Choi, N.Y. Yang, Soot graphitic order in laminar diffusion flames and a large-scale JP-8 pool fire, Int. J. Heat Mass Tran. 48 (2005) 3604-3614.

[38] R.J. Santoro, T.T. Yeh, J.J. Horvath, H.G. Semerjian, The transport and growth of soot particles in laminar diffusion flames, Combust. Sci. Technol. 53 (1987) 89-115.

[39] L.G. Blevins, R.A. Fletcher, B.A. Benner, E.B. Steel, G.W. Mulholland, The existence of young soot in the exhaust of inverse diffusion flames, Proc. Combust. Inst. 29 (2002) 2325-2333.

[40] K.T. Kang, J.Y. Hwang, S.H. Chung, W. Lee, Soot zone structure and sooting limit in diffusion flames: Comparison of counterflow and co-flow flames, Combust. Flame 109 (1997) 266-281.

[41] K.T. Wu, R.H. Essenhigh, Mapping and structure of inverse diffusion flames of methane, Proc. Combust. Inst. 20 (1985) 1925-1932.

[42] X. Zhu, X. Xia, P. Zhang, Near-field Flow Stability of Buoyant Methane/Air Inverse Diffusion

Flames, Combust. Flame 191 (2018) 66-75.

[43] F.F. Grinstein, K. Kailasanath, Three-dimensional numerical simulations of unsteady reactive square jets, Combust. Flame 100 (1995) 2-10.

[44] F.F. Grinstein, K. Kailasanath, Exothermicity and three-dimensional effects in unsteady propane square jets, Proc. Combust. Inst. 26 (1996) 91-96.

[45] K.R. Anderson, S. Mahalingam, J. Hertzberg, A two-dimensional planar computational investigation of flame broadening in confined non-premixed jets, Combust. Flame 118 (1999) 233-247.

[46] Y.C. Chao, C.Y. Wu, A study of the interaction between a jet flame and a lateral wall, Combust. Sci. Technol. 158 (2000) 93-113.

[47] X. Jiang, K.H. Luo, Dynamics and structure of transitional buoyant jet diffusion flames with side-wall effects, Combust. Flame 133 (2003) 29-45.

[48] H.G. Weller, G. Tabor, H. Jasak, C. Fureby, A tensorial approach to computational continuum mechanics using object-oriented techniques, Comp. Phys. 12 (1998) 620-631.

[49] R.I. Issa, Solution of the implicitly discretised fluid flow equations by operator-splitting, J. Comput. Phys. 62 (1986) 40-65.

[50] H. Jasak, Error analysis and estimation for finite volume method with applications to fluid flow, Ph.D. thesis, Imperial College, University of London (1996).

[51] B.P. Leonard, Simple high‐accuracy resolution program for convective modelling of discontinuities, Int. J. Numer. Methods Fluids 8 (1988) 1291-1318.

[52] T. Poinsot, D. Veynante, Theoretical and numerical combustion, RT Edwards, Inc.2005.

[53] A. Yoshizawa, K. Horiuti, A statistically-derived subgrid-scale kinetic energy model for the large-eddy simulation of turbulent flows, Journal of the Physical Society of Japan 54 (1985) 2834-2839.

[54] S. Menon, P.-K. Yeung, W.-W. Kim, Effect of subgrid models on the computed interscale energy transfer in isotropic turbulence, Fluid Dynamics Conference, 1996, pp. 2387.

[55] C.K. Law, Combustion physics, Cambridge university press2010.

[56] C.S. McEnally, Ü.Ö. Köylü, L.D. Pfefferle, D.E. Rosner, Soot volume fraction and temperature measurements in laminar nonpremixed flames using thermocouples, Combustion and Flame 109 (1997) 701-720.

[57] D. Bradley, A. Entwistle, Determination of the emissivity, for total radiation, of small diameter Platinum-10% Rhodium wires in the temperature range 600-1450 C, British Journal of Applied Physics 12 (1961) 708.

[58] C.R. Shaddix, Correcting thermocouple measurements for radiation loss: a critical review, Sandia National Labs., Livermore, CA (US), 1999.

[59] B.M. Cetegen, T.A. Ahmed, Experiments on the periodic instability of buoyant plumes and pool fires, Combust. Flame 93 (1993) 157-184.

[60] T.L. Doligalski, C.R. Smith, J.D.A. Walker, Vortex interactions with walls, Ann. Rev. Fluid Mech. 26 (1994) 573-616.

[61] A. Luton, S. Ragab, D. Telionis, Interaction of spanwise vortices with a boundary layer, Phys. Fluids 7 (1995) 2757-2765.

[62] C.C. Chu, C.T. Wang, C.C. Chang, A vortex ring impinging on a solid plane surface—Vortex structure and surface force, Phys. Fluids 7 (1995) 1391-1401.